Parametrization and validation of a nonsmooth discrete element method for simulating flows of iron ore green pellets

D. Wang[a], M. Servin[b], T. Berglund[c], K-O. Mickelsson[d], S. Rönnbäck[e]

[a] *Umeå University, Umeå, Sweden.*
[b] *Umeå University, Umeå, Sweden (martin.servin@physics.umu.se).*
[c] *Algoryx Simulation AB, Umeå, Sweden.*
[d] *LKAB R&D, Malmberget, Sweden.*
[e] *Optimation AB, Luleå, Sweden.*

Abstract

The nonsmooth discrete element method (NDEM) have the potential of high computational efficiency for rapid exploration of large design space of systems for processing and transportation of mineral ore. We present parametrization, verification and validation of a simulation model based on NDEM for iron ore green pellet flow in balling circuits. Simulations are compared with camera based measurements of individual pellet motion as well as bulk behaviour of pellets on conveyors and in rotating balling drum. It is shown that the NDEM simulation model is applicable for the purpose of analysis, design and control of iron ore pelletizing systems. The sensitivity to model and simulation parameters is investigated. It is found that: the errors associated with large time-step integration do not cause statistically significant errors to the bulk behaviour; rolling resistance is a necessary model component; and the outlet flow from the drum is sensitive to fine material adhering to the outlet creating a thick coating that narrows the outlet gaps.

Keywords: granular materials; discrete element method; validation; iron ore pellets; pelletizing; balling circuit
2010 MSC: 00-01, 99-00

1. Introduction

Numerical simulation of granular materials is an important tool both for advancing the fundamental understanding of many natural phenomena in material science and geophysics, and for the design, control and optimization of systems for processing, manufacturing, storage and transportation of granular materials, e.g., grains, corn, pharmaceuticals pills, pellets, soil and minerals. In the mineral processing industry, experiments and *in situ* measurements are many times prohibitive for practical and economical reasons, and in these cases,

modeling and simulation play an essential role in finding deeper understanding of the process, making radical improvements and innovating entirely new solutions.

Parametrization, verification and validation are critical steps for making sure that the simulation model provides a sufficiently accurate representation of the real system. By parametrization we mean the process of identifying numerical values of the model parameters from observations of the real system. By the verification it is established that the computer simulation reproduces the mathematical model. A failure indicates either a flaw in the numerical method or in the software implementation. Validation is testing the agreement between the simulated model and the real system. This determines the predictive power of the simulated model to some given degree of accuracy of a selected set of observables. A significant disagreement implies that the model is not useful for describing the systems behaviour.

We consider the use of large-scale granular matter simulation based on the nonsmooth discrete element method (NDEM) [1, 2] for the design of balling drum outlets [3] used in iron ore pelletizing [4]. The NDEM have the potential of high computational efficiency compared to conventional (smooth) DEM. This enables rapid exploration of the design space. The NDEM is on the other hand not as well tested as conventional DEM for industry applications and scarcely put to validation tests. In this paper we present procedure and results for parametrization of the properties of green iron ore pellets and validation of the macroscopic bulk behaviour by comparing the numerical simulations with camera based measurements. The measurements include tracking of individual iron ore green pellets and characterization of bulk behaviour in an industrial pelletizing system. The goal is to establish the predictive power of NDEM simulations for the purpose of design and control of pelletizing systems, including the sensitivity of the flow characteristics with respect to certain model parameters. The NDEM method in [2] is also extended to include a constraint based rolling resistance which is shown to be crucial for the material distribution of iron ore green pellets.

2. Background

2.1. Iron ore pelletizing

The iron ore pelletizing process usually has the following main stages [4]. Comminuted fine size ore, *fines*, is first mixed with binder material. Agglomeration into soft ore balls, *green ore pellets*, occur in balling circuits where fines, water and undersized pellets are fed into rotating drums. In the drum flow the green pellets are mixed with fine material and grow by layering and coalescence. New pellets are formed by nucleation. The drum is slightly inclined to produce an axial flow. The green pellets leave the drum through an outlet and are size distributed on a roller sieve, see Fig. 2. Under-sized particles are fed back to the drum. Over-sized pellets are crushed and mixed with the fines. On-sized pellets (9 to 16 mm in diameter) are conveyed to the induration furnace where

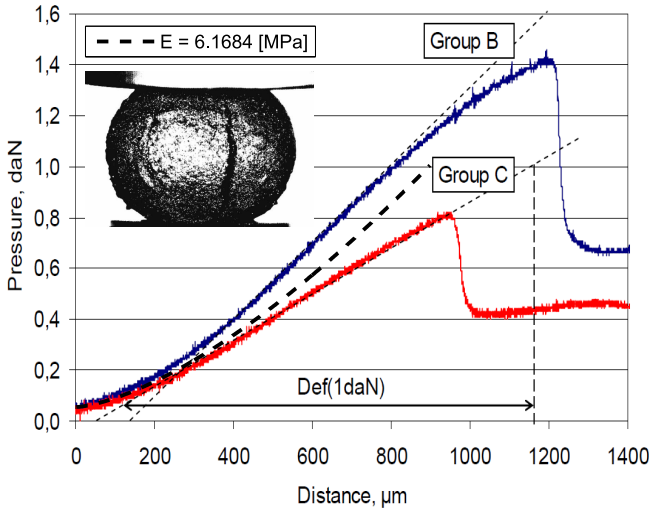

Figure 1: Measurement of elasticity and strength of iron ore green pellets from Forsmo *et al* in Ref. [20] Fig. 1 and 13c.

they form hard pellets by oxidation and sintering. After this stage the cooled pellets are ready for transportion to distant steelmills. A typical iron ore balling circuit may have drum diameter ranging between $3-5$ m and $8-10$ m long and circulate about $400-1200$ ton/h producing $100-300$ ton/h on-size pellets.

The mathematical modeling of granulation systems was reviewed in Ref. [5]. A smooth DEM simulation model of iron ore granules in a continuous drum mixer was developed in [6] to analyse the flow dependence on drum design (angle and length). In [3] a methodology based on the nonsmooth discrete element method (NDEM) was presented for simulation based design of drum outlets, for even flow profile of ore green pellets on to the roller sieve. Fig. 2 show an image from outlet analysis using NDEM simulation. The simulation demonstrate that the original outlet design was far from optimal as the material distribution on the wide-belt conveyor is inhomogeneous. As an effect, the roller sieve cannot be used efficiently. Furthermore, the green pellets may be damaged by the pressure from building a too thick pellet bed. A simulation model for the analysis and design of the balling process must be able to predict the flow and distribution of material both inside the balling drum and on the conveyor belt below the outlet.

2.2. Nonsmooth discrete element methods

In the conventional discrete element method (DEM) the granules are modeled as rigid bodies interacting by contact forces modeled as linear or non-linear damped springs. We refer to this as *smooth* DEM as it involves the numerical integration of smooth (but usually stiff) ordinary differential equations. The computational aspects of smooth DEM is covered in Ref. [7]. In the *nonsmooth*

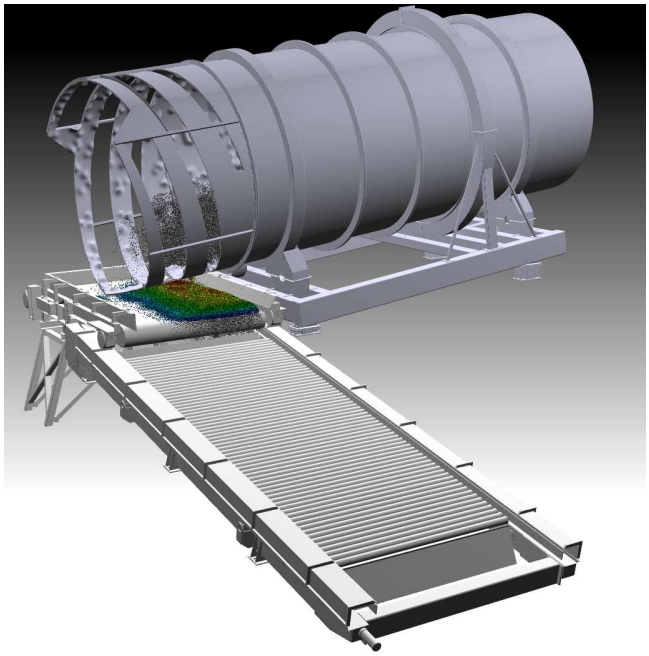

Figure 2: Image from simulation of balling drum with green ore pellets flowing through the outlet gaps onto the wide-belt conveyor feeding the roller sieve.

DEM [8, 9, 1], impacts and frictional stick-slip transitions are considered as instantaneous events making the velocities discontinuous in time. The contact forces and impulses are modeled in terms of kinematic constraints and complementarity conditions between constraint forces and contact velocities, e.g., by the Signorini-Coulomb law for unilateral non-penetration and dry friction. The contact network become strongly coupled and any dynamic event may propagate through the system instantaneously. The benefit of nonsmooth DEM is that it allows integration with much larger simulation step-size than for smooth DEM and is thus potentially faster.

We use a regularized version of nonsmooth DEM referred to as *semi-smooth* DEM in Ref. [2], which combines the numerical stability at large step-size with the possibility of modeling the viscoelastic nature of the contact forces and mapping the simulation parameters to the conventional material parameters. The constrained equations of motion, between impacts, are

$$\begin{aligned} \mathbf{M}\dot{\mathbf{v}} + \dot{\mathbf{M}}\mathbf{v} &= \mathbf{f}_{\text{ext}} + \mathbf{G}_{\text{n}}^{\text{T}}\boldsymbol{\lambda}_{\text{n}} + \mathbf{G}_{\text{t}}^{\text{T}}\boldsymbol{\lambda}_{\text{t}} && (1)\\ 0 \le \varepsilon_{\text{n}}\boldsymbol{\lambda}_{\text{n}} + \mathbf{g}_{\text{n}}(\mathbf{x}) &\perp \boldsymbol{\lambda}_{\text{n}} \ge 0 && (2)\\ \gamma_{\text{t}}\boldsymbol{\lambda}_{\text{t}} + \mathbf{G}_{\text{t}}(\mathbf{x})\mathbf{v} &= 0 && (3)\\ |\boldsymbol{\lambda}_{\text{t}}^{(\alpha)}| &\le \mu|\mathbf{G}_{\text{n}}^{(\alpha)\text{T}}\lambda_{\text{n}}^{(\alpha)}| && (4) \end{aligned}$$

where $\mathbf{x}$, $\mathbf{v}$ and $\mathbf{f}_{\text{ext}}$ are global vectors of position, velocity and external force, and $\mathbf{M}$ is the system mass matrix. Rotational degrees of freedom are included such that $\mathbf{v}$ and $\mathbf{f}_{\text{ext}}$ are vectors of dimension $6N_{\text{p}}$ including components of angular velocity and torque. The constraint forces for maintaining the non-penetration constraint and Coulomb friction are $\mathbf{G}_{\text{n}}^{\text{T}}\boldsymbol{\lambda}_{\text{n}}$ and $\mathbf{G}_{\text{t}}^{\text{T}}\boldsymbol{\lambda}_{\text{t}}$, where $\boldsymbol{\lambda}_{\text{n}}$ and $\boldsymbol{\lambda}_{\text{t}}$ are the Lagrange multipliers for the normal (n) and tangential (t) directions of each contact plane. The corresponding contact Jacobians are $\mathbf{G}_{\text{n}}$ and $\mathbf{G}_{\text{t}}$. In absence of regularization the constraints express non-penetration, $\delta \ge 0$, where δ is the gap function, and no-slip, $\mathbf{G}_{\text{t}}\mathbf{v} = 0$. The constraints can be regarded as the limit of infinitely strong potentials and dissipation functions $U_\varepsilon(\boldsymbol{x}) = \frac{1}{2\varepsilon}\boldsymbol{g}^T\boldsymbol{g}$ and $\mathcal{R}_\gamma(\boldsymbol{x}, \dot{\boldsymbol{x}}) = \frac{1}{2\gamma}\bar{\boldsymbol{g}}^T\bar{\boldsymbol{g}}$ with $\varepsilon, \gamma \to 0$ [10, 12]. Eq. (2) and (3) are the regularized versions of non-penetration and no-slip, with regularization parameters ε_{n} and γ_{t}. We use finite regularization and map the non-penetration constraint, for each contact α with gap function $\delta_{(\alpha)}$, to the Hertz contact force law, $f_{(\alpha)} = k_{\text{n}}\delta_{(\alpha)}^{3/2}$, by defining $g_{\text{n}}^{(\alpha)} \equiv \delta_{(\alpha)}^{e_{\text{H}}}$ with exponent $e_{\text{H}} = 5/4$. This maps the regularization parameter to the Hertz spring coefficient and conventional material parameters as $\varepsilon_{\text{n}} = e_{\text{H}}/k_{\text{n}} = 3e_{\text{H}}(1-\nu^2)/E\sqrt{r^*}$, where E is the Young's modulus, ν the Poisson ratio and r^* is the effective contact radius. Similarly, a dissipation term, $\gamma_{\text{n}}\mathbf{G}_{\text{n}}\mathbf{v}$, may also be added to the normal constraint multiplier condition (2). This produce a viscous damping force term, $f_{\text{d}} = k_{\text{n}}c\sqrt{\delta}\dot{\delta}$, in Hertz contact law with the damping parameter defined as $\gamma_{\text{n}} = e_{\text{H}}^2/k_{\text{n}}c$, which relates it also to the physical viscosity constant η by $c = 4(1-\nu^2)(1-2\nu)\eta/15E\nu^2$ [11]. See Ref. [2] for details on the mapping of regulization parameters. The friction constraint impose zero tangential contact velocity, $\mathbf{G}_{\text{t}}^{(\alpha)}\mathbf{v}_{(\alpha)} = 0$, unless the tangent force reach the friction bounds set by the Coulomb law, Eq. (4). The

tangent plane is spanned with two orthogonal vectors $\mathbf{t}_1^{(\alpha)}$ and $\mathbf{t}_2^{(\alpha)}$ resulting in friction multiplier having two components $\boldsymbol{\lambda}_{\rm t}^{(\alpha)} = [\boldsymbol{\lambda}_{\rm t_1}^{(\alpha)}\ \boldsymbol{\lambda}_{\rm t_2}^{(\alpha)}]^{\rm T}$. When impacts occur, the equations of motion are supplemented by the Newton impact law, $\mathbf{G}_{\rm n}^{(\alpha)}\mathbf{v}_+ = -e\mathbf{G}_{\rm n}^{(\alpha)}\mathbf{v}_-$, with coefficient of restitution e.

For numerical time integration we use the SPOOK stepper [12] derived from discrete variational principle for the augmented system $(\mathbf{x}, \mathbf{v}, \boldsymbol{\lambda}, \dot{\boldsymbol{\lambda}})$. Stepping the system position and velocity, $(\mathbf{x}_i, \mathbf{v}_i) \to (\mathbf{x}_{i+1}, \mathbf{v}_{i+1})$, from time t_i to $t_{i+1} = t_i + \Delta t$ involve solving a mixed linear complementarity problem (MLCP) [13] of the form

$$\begin{gathered} \mathbf{H}\mathbf{z} + \mathbf{b} = \mathbf{w}_l - \mathbf{w}_u \\ 0 \le \mathbf{z} - \mathbf{l} \perp \mathbf{w}_l \ge 0 \\ 0 \le \mathbf{u} - \mathbf{z} \perp \mathbf{w}_u \ge 0 \end{gathered} \tag{5}$$

where

$$\mathbf{H} = \begin{bmatrix} \mathbf{M} & -\mathbf{G}_{\rm n}^{\rm T} & -\mathbf{G}_{\rm t}^{\rm T} \\ \mathbf{G}_{\rm n} & \boldsymbol{\Sigma}_{\rm n} & 0 \\ \mathbf{G}_{\rm t} & 0 & \boldsymbol{\Sigma}_{\rm t} \end{bmatrix}, \quad \mathbf{z} = \begin{bmatrix} \mathbf{v}_{i+1} \\ \boldsymbol{\lambda}_{{\rm n},i+1} \\ \boldsymbol{\lambda}_{{\rm t},i+1} \end{bmatrix}, \quad \mathbf{b} = \begin{bmatrix} -\mathbf{M}\mathbf{v}_i - \Delta t\mathbf{M}^{-1}\mathbf{f}_{\rm ext} \\ \frac{4}{\Delta t}\boldsymbol{\Upsilon}_{\rm n}\mathbf{g}_{\rm n} - \boldsymbol{\Upsilon}_{\rm n}\mathbf{G}_{\rm n}\mathbf{v}_i \\ 0 \end{bmatrix} \tag{6}$$

and the solution vector $\mathbf{z}$ contains the new velocities and the Lagrange multipliers $\boldsymbol{\lambda}_{\rm n}$ and $\boldsymbol{\lambda}_{\rm t}$. For notational convenience, a factor Δt has been absorbed in the multipliers such that the constraint force reads $\mathbf{G}^T\boldsymbol{\lambda}/\Delta t$. The diagonal matrices $\boldsymbol{\Sigma}_{\rm n}$, $\boldsymbol{\Sigma}_{\rm t}$ and $\boldsymbol{\Upsilon}_{\rm n}$ are given in Appendix A in terms of the viscoelastic material parameters. The upper and lower limits, u and l in Eq. (6), follow from Signorini-Coulomb law including $0 \le \lambda_{\rm n}^{(\alpha)}$ and $|\boldsymbol{\lambda}_{\rm t}^{(\alpha)}| \le \mu_{\rm s}|\mathbf{G}_{\rm n}^{(\alpha)\rm T}\boldsymbol{\lambda}_{\rm n}^{(\alpha)}|$ with the friction coefficient $\mu_{\rm s}$. w_l and w_u are temporary slack variables. Impacts are treated *post facto*. After stepping the velocities and positions an impact stage follows. This include solving a MLCP similar to Eq. (5) but with the Newton impact law, $\mathbf{G}_{\rm n}^{(\alpha)}\mathbf{v}_+ = -e\mathbf{G}_{\rm n}^{(\alpha)}\mathbf{v}_-$, replacing the normal constraints for the contacts with normal velocity larger than an impact velocity threshold $v_{\rm imp}$. The remaining constraints are maintained by imposing $\mathbf{G}\mathbf{v}_+ = 0$.

We use a projected Gauss-Seidel (PGS) algorithm, as described in Ref. [2] and summarized in Appendix A, for solving the MLCP (5). The method is implemented in the software AgX Dynamics [14]. The time-step Δt should be chosen

$$\Delta t \lesssim \min(\epsilon d/v_{\rm n}, \sqrt{2\epsilon d/g}) \tag{7}$$

for contact error threshold ϵ, where $v_{\rm n}$ is the characteristic relative normal contact velocity and $g_{\rm acc} = 9.82\ {\rm m/s^2}$ is the gravitational acceleration. We set the impact velocity threshold to $v_{\rm imp} = \epsilon d/\Delta t$. The required number of PGS iterations depend on the size and configuration of the contact network. For bulk systems a rough rule is $N_{\rm it} = 0.1 \times n/\epsilon$, where n is the length of the contact network (number of contacts) in the direction of gravity [2]. The computational time $t_{\rm comp}$ per simulated time $t_{\rm real}$ is

$$t_{\rm comp} = \frac{\Omega}{h} t_{\rm real} \tag{8}$$

where $\Omega = K_{\text{cpu}} N_{\text{it}} \alpha_{\text{p}} N_{\text{p}} / N_{\text{cpu}}$, α_{p} is the average number of contacts per particle, N_{cpu} the number of cpu cores and K_{cpu} the average computational time for a single PGS update. We measure $K_{\text{cpu}} \approx 1^{-6}$ s with a desktop computer with Intel(R) Core(TM) Xeon X5690, 3.46 GHz, 48 GB RAM on a Linux 64 bit system. The PGS implementation parallelizes well up to 8 cores but saturates beyond that.

2.3. Rolling resistance constraint

There are several physical causes for rolling resistance, see, e.g., Ref. [15]. These include the effect of particle shape deviating from a spherical idealization, plastic or viscous deformations of the object itself or in the contact interface, frictional slippage in the contact interface and surface adhesion. In the idealization of rigid bodies, rolling resistance may be modeled as a torque, $\boldsymbol{\tau}_{\text{r}}$, on the contacting bodies counteracting their relative rolling motion. Similarly to Coulomb friction, the rolling resistance torque is limited in magnitude by $|\boldsymbol{\tau}_{\text{r}}| \leq \mu_{\text{r}} r^*_{ab} |\mathbf{f}_{\text{n}}|$, where $0 \leq \mu_{\text{r}}$ is the *rolling resistance coefficient*, $r^*_{ab} = r_a r_b / (r_a + r_b)$ is the *effective contact radius* of two contacting geometries a and b. When the source of rolling resistance is purely geometric the rolling resistance coefficient can be derived from the shape. For octagon shape $\mu_{\text{r}} = 0.1$ [16]. Rolling resistance is important to include for correct prediction of single particle motion as well as for the collective behaviour of granular materials, e.g., formation of stable piles with accurate angle of repose, stress and strain relationships in dense packings and the shear rate in flowing systems. An overview of the conventional smooth DEM models and their agreement with experiments is found in Ref. [15]. Some rolling resistance models in smooth DEM work well for quasi-static systems while poorly for flowing systems and vice versa. In nonsmooth DEM, where the contact forces and dynamics are computed implicitly, e.g., as kinematic constraints, a single model can be used for both regimes. Only a few models of rolling resistance for nonsmooth DEM can be found in literature [17, 18, 19] and no reported results concerning parametrization and validation with experimental data.

We extend the nonsmooth DEM model by including additional rolling resistance constrains in Eq. (5) of the form $\mathbf{G}_{\text{r}}\mathbf{v} = 0$ and constraint force (torque) $\boldsymbol{\tau}_{\text{r}} = \mathbf{G}_{\text{r}}^T \boldsymbol{\lambda}_{\text{r}} / h$. Consider a contact α between two granules, a and b, with linear and angular velocity vectors denoted $\mathbf{u}$ and $\boldsymbol{\omega}$. Let the contact plane have unit normal $\mathbf{n}$ and orthonormal tangents $\mathbf{t}_1$ and $\mathbf{t}_2$. This is illustrated in Fig. 3. The condition for zero relative rolling velocity can be expressed

$$\mathbf{0}_{3\times 1} = \begin{bmatrix} \mathbf{t}_1^{\text{T}}(\boldsymbol{\omega}_a - \boldsymbol{\omega}_b) \\ \mathbf{t}_2^{\text{T}}(\boldsymbol{\omega}_a - \boldsymbol{\omega}_b) \\ \mathbf{n}^{\text{T}}(\boldsymbol{\omega}_a - \boldsymbol{\omega}_b) \end{bmatrix} = \underbrace{\begin{bmatrix} \mathbf{0}_{1\times 3} & \mathbf{t}_1^{\text{T}} & \mathbf{0}_{1\times 3} & -\mathbf{t}_1^{\text{T}} \\ \mathbf{0}_{1\times 3} & \mathbf{t}_2^{\text{T}} & \mathbf{0}_{1\times 3} & -\mathbf{t}_2^{\text{T}} \\ \mathbf{0}_{1\times 3} & \mathbf{n}^{\text{T}} & \mathbf{0}_{1\times 3} & -\mathbf{n}^{\text{T}} \end{bmatrix}}_{\mathbf{G}_{\text{r}}} \begin{bmatrix} \mathbf{u}_a \\ \boldsymbol{\omega}_a \\ \mathbf{u}_b \\ \boldsymbol{\omega}_b \end{bmatrix} \tag{9}$$

from which we identify the constraint Jacobian for rolling resistance. By the geometry of the Jacobian it is clear that this constraint force is indeed a torque.

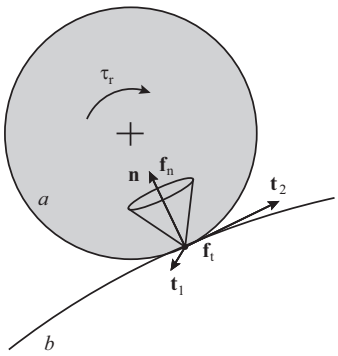

Figure 3: Illustration of two contacting granular geometries a and b. Rolling resistance constraint produce a torque, $\boldsymbol{\tau}_{\mathrm{r}}$, limited in magnitude relative to the normal contact force $\boldsymbol{f}_{\mathrm{n}}$ in a similar way as the Coulomb friction force $\boldsymbol{f}_{\mathrm{t}}$.

Table 1: Identified iron ore green pellet parameters.

ρ	3700 kg/m^3	mass density
d	12.7 ± 3 mm	diameter
E	6.2 ± 0.7 MPa	Young's modulus
e	0.18 ± 0.04	coefficient of restitution
μ_{s}	0.91 ± 0.04	surface friction coefficient
μ_{r}	0.32 ± 0.02	rolling resistance coefficient

We denote the components of the multiplier $\boldsymbol{\lambda}_{\mathrm{r}} = (\lambda_{\mathrm{r}t_1}, \lambda_{\mathrm{r}t_2}, \lambda_{\mathrm{r}n})^T$. The third constraint $0 = \mathbf{n}^{\mathrm{T}}(\boldsymbol{\omega}_a - \boldsymbol{\omega}_b)$ oppose relative twisting and produce torsional force. We linearize the limits on the torque, $|\boldsymbol{\tau}_{\mathrm{r}}| \leq \mu_{\mathrm{r}} r^*_{ab} |\mathbf{f}_{\mathrm{n}}|$, and obtain additional multiplier conditions to Eq. (5)

$$-\mu_{\mathrm{r}} r^*_{ab} \lambda_{\mathrm{n}} \leq \quad \lambda_{\mathrm{r}t_1} \leq \quad \mu_{\mathrm{r}} r^*_{ab} \lambda_{\mathrm{n}} \tag{10}$$

$$-\mu_{\mathrm{r}} r^*_{ab} \lambda_{\mathrm{n}} \leq \quad \lambda_{\mathrm{r}t_2} \leq \quad \mu_{\mathrm{r}} r^*_{ab} \lambda_{\mathrm{n}} \tag{11}$$

$$-\alpha_{\mathrm{r}n} \mu_{\mathrm{s}} r^*_{ab} \lambda_{\mathrm{n}} \leq \quad \lambda_{\mathrm{r}n} \leq \quad \alpha_{\mathrm{r}n} \mu_{\mathrm{s}} r^*_{ab} \lambda_{\mathrm{n}} \tag{12}$$

where $\alpha_{\mathrm{r}n}$ is a factor depending on shape with value zero for perfect spheres and up to 1 for shapes with contact surface area as for a cube. A regularization term $\boldsymbol{\Sigma}_{\mathrm{r}}$ is added to the new diagonal block in $\mathbf{H}$, see Appendix A, and the corresponding components in $\boldsymbol{b}$ are set to zero.

3. Identification of iron ore green pellet parameters

The identified parameters for onsize iron ore green pellets are summarized in Table 1.

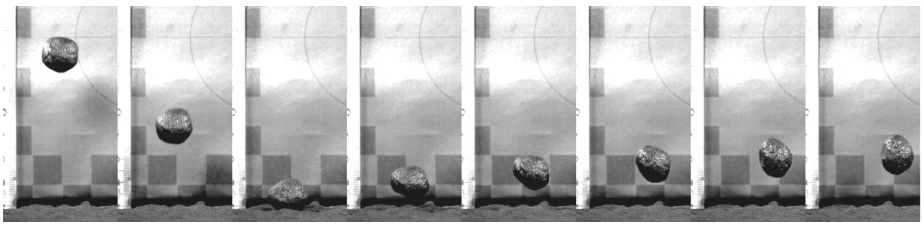

Figure 4: Measurement of coefficient of restitution by impacting ore green pellet captured at 100 Hz.

3.1. Mass and geometry

Iron ore green pellet have mass density of about 3700 kg/m^3. The shape is approximately spherical with diameter ranging between 9 and 16 mm and *shape factor*[1] in the range $0.7 - 0.95$.

3.2. Elasticity

The elasticity and strength of iron ore green pellets was investigated by Forsmo *et al* [20]. Assuming a relation between pressure force f_n and compression δ of the form of Hertz contact law, $f_\mathrm{n} = k_\mathrm{n}\delta^{3/2}$, we identify $k_\mathrm{n} = (0.35 \pm 0.05) \times 10^6$, which translates to Young's modulus $E = 3k_\mathrm{n}(1-\nu^2)/\sqrt{2d} = 6.2 \pm 0.7$ MPa , see Fig. 1. We assume Poisson ratio $\nu = 0.25$.

3.3. Restitution

The coefficient of restitution is identified from drop tests where ore green pellets impact on a surface coated with a 10 mm thick layer of ore material packed to similar density as of ore green pellets, see Fig. 4. The green pellet was released from height 0.45 m and bounces to a height of 12 ± 4 mm, which implies an impact velocity $v^- = 2.97$ m/s and a post impact velocity $v^+ = 0.49 \pm 0.08$ m/s. The coefficient of restitution $e = -v^+/v^-$ is thus found to be $e = 0.18 \pm 0.04$.

3.4. Surface friction

The friction coefficient, μ_s, between two ore surfaces is identified by measuring the required force f for pulling a block of packed ore over a surface of packed ore, see Fig. 5. From the Coulomb law, $f = \mu_\mathrm{s} m g_\mathrm{acc}$, we find $\mu_\mathrm{s} = 0.91 \pm 0.04$

3.5. Rolling resistance

The rolling resistance coefficient is determined from observing the angle ϕ_r at which the ore green pellet starts to roll down an inclined plane. We observe $\phi_\mathrm{r} = 17.8 \pm 0.1^\circ$. With $\boldsymbol{\tau}_\mathrm{r} = (d/2)\sin(\phi_\mathrm{r}) f_\mathrm{n}$ we thus identify the rolling resistance coefficient to $\mu_\mathrm{r} = 0.32 \pm 0.02$.

[1]The shape factor of a cross-section of area A and perimeter length L is $4\pi A/L^2$. A sphere has shape factor 1 and a square has roughly 0.78.

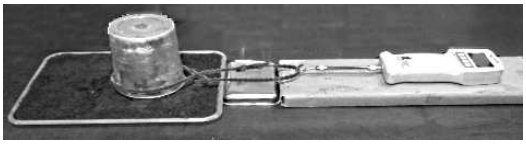


Figure 5: Measurement of surface friction (left) and rolling resistance (right).

Table 2: Summary of results from verification tests.

Test	**Quantity**	**Result**	**Comment**
Elasticity	$\|k_{\text{eff}} - k\|/k$	$0 - 2\%$	error 2% at $\rho/d \gtrsim 0.1$ and $\Delta t \gtrsim 5$ ms
Restitution	$\|e_{\text{eff}} - e\|/e$	1%	$\Delta t \lesssim \min(\epsilon d/v_{\text{n}}, \sqrt{2\epsilon d/g})$ and $\epsilon = 0.01$
Friction	$\|\mu_{\text{eff}} - \mu\|/\mu$	0%	fulfilled to machine precision
Rolling resistance	$\|\mu_{\text{r,eff}} - \mu_{\text{r}}\|/\mu_{\text{r}}$	$0 - 1\%$	1% error at rolling onset.

4. Verification of simulated pellets

Material parameters in Table 1 are translated to simulation parameters of NDEM according to Sec. 2.2 and verified in elementary tests described below. The results are summarized in Table 2. Simulation parameters are set to $\Delta t = 0.01$ s, $N_{\text{it}} = 150$ if nothing else is stated.

4.1. Elasticity

The elasticity model is verified in simulation by compressing a pellet between a moving piston and a static plane. The piston moves in 0.02 mm/s towards to the plane. The measured constraint force $\mathbf{G}_{\text{n}}^{\text{T}}\boldsymbol{\lambda}_{\text{n}}/\Delta t$ coincide with the Hertz model with an effective elasticity coefficient $k_{\text{eff}} = f_{\text{n}}/\delta^{3/2}$ deviating from k_{n} with maximally 2% at $\delta/d = 0.1$ for time step $\Delta t = 5$ ms. The deviation decrease for smaller overlap and with decreasing time step. In the case of a single particle compressed towards to the static ground by external force, the result match to machine precision.

4.2. Restitution

The impact model is verified by measuring the re-bounce height h_{b} from dropping particles from height h_{d} and computing the effective coefficient of restitution $e_{\text{eff}} = \sqrt{h_{\text{b}}/h_{\text{d}}}$. The impact stage reproduce the impact law $v_+ = -ev_-$ to machine precision. However, finite time-stepping cause impact overlaps of magnitude $\delta \leq \Delta t v_+$. This produce errors in the particle trajectories of the same order. Furthermore, the division of contacts into an impact stage and continuous contact stage can produce residual energy at contact separation that cause violation of the impact law. Thus, the effective dissipation can be smaller than predicted by the impact law, i.e., the effective restitution become bigger. The effect is more notable for low-restitution materials and appears as an

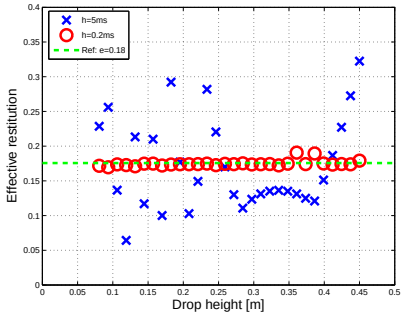

Figure 6: Verification of the impact model by measuring the effective restitution.

effective restitution larger than e. The test is performed for drop height ranging up to 0.45 m and time step 5 ms and 0.2 ms. The results are shown in Fig. 6. The effective restitution become 0.17 ± 0.07 and 0.175 ± 0.004, respectively. Note that given the drop-height 0.45 m and an error tolerance of $\epsilon = 2\%$, the time-step rule $\Delta t \lesssim \epsilon d/v_{\mathrm{n}}$ imply $\Delta t = 0.4$ ms. The time-step 5 ms, on the other hand, correspond to an error tolerance of $\epsilon = 100\%$. The verification results are thus in good agreement with these error estimates but it is clear that using too large time-step may cause significant errors in energy dissipation at impacts.

4.3. Surface friction

The surface friction model is verified by simulating a pellet being pressed towards a static plane and pulled horizontally until it starts to slide. The effective friction coefficient is computed as the ratio of the horizontally applied force at slide onset over applied normal pressure, $\mu_{\mathrm{s,eff}} = f_{\mathrm{t}}/f_{\mathrm{n}}$. The result agree with μ_{s} to machine precision.

4.4. Rolling resistance

As verification of rolling resistance we measure the maximum angle ϕ_{r} where a simulated ore green pellet doesn't start rolling on an inclined plane and compute the effective rolling resistance coefficient $\mu_{\mathrm{r,eff}} = \sin(\phi_{\mathrm{r}})$. The result is $\phi_{\mathrm{r}} = 17.84^{\circ}$ and $\mu_{\mathrm{r,eff}} = 0.31$, to be compared to the corresponding values $17.8 \pm 1^{\circ}$ and 0.32 from experiment. The discrepancy is due to truncation error of the residual in the Gauss-Seidel solver but is of no practical significance to the results in the paper. As a complementary verification test, we simulate the deceleration of a fast rolling pellet on a horizontal plane assuming no-slip. The result agree with the analytical solution $\dot{v} = -\frac{5}{7}\mu_{\mathrm{r}} g_{\mathrm{acc}}$ to machine precision.

5. Observed bulk behaviour of iron ore green pellets

We use two on-line production balling circuits at LKAB pelletizing plant in Malmberget, Sweden, for observation and validation of iron ore green pellet

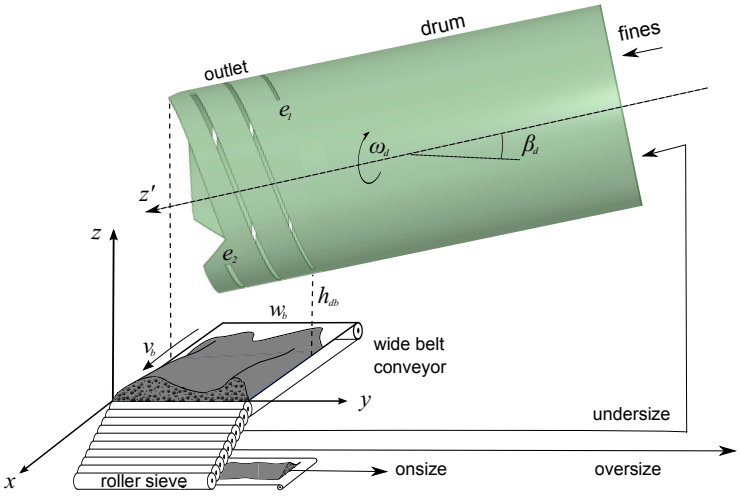

Figure 7: Illustration of the balling circuit.

Table 3: Specification of balling circuit parameters.

Notation	**Value**	**Parameter**
ω_d	0.53 rad/s	drum rotation speed
β_d	7°	drum inclination
D	3.7 m	drum inner diameter
L	8.1 m	drum length
$\{e_1 : e_2\}$	$\{4.7 : 7.9\}$ d	inner : outer gap width
w_b	2.4 m	width of wide-belt conveyor
v_b	0.19 m/s	speed of wide-belt conveyor
h_db	0.45 m	distance drum to conveyor
$\dot{M}_\mathrm{RK1}$	340 ton/h	mass flow rate in RK1
$\dot{M}_\mathrm{RK5}$	275 ton/h	mass flow rate in RK5

bulk behaviour. The circuits, referred to as RK1 and RK5, are identical but run with different feed rate. The balling process was described in Sec. 2.1 and the balling circuit is illustrated in Fig. 7. The key parameters are given in table 3. We observe and validate three bulk properties: the angle of repose of static piles on the conveyor of on-size pellets, the properties of the flow inside the balling drum and the spatial distribution of material on the wide-belt conveyor that results from the interaction of the flow with the outlet geometry.

5.1. Pile shape

The resting angle of repose, θ_r, is measured on the conveyor belt transporting on-size green pellets from the balling circuit to the induration furnace. An elongated pile is formed on the conveyor by feeding material from another conveyor, aligned perpendicularly to the first. The drop height is 0.3 m and feed

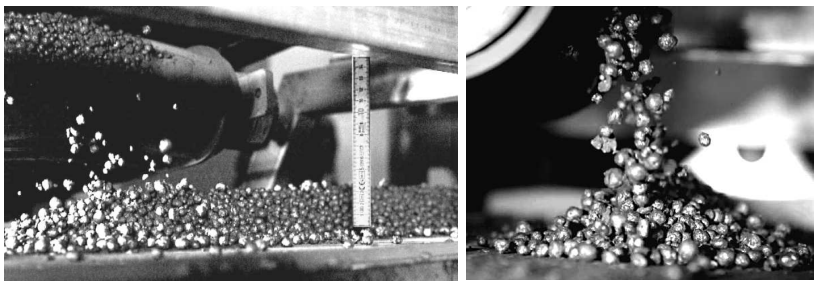

Figure 8: Photos from angle of repose measurement.

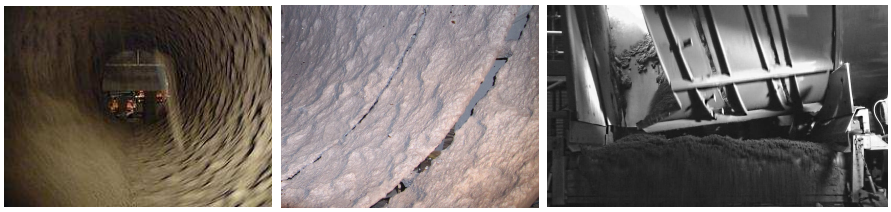

Figure 9: Sample images of drum interior (left and middle) and distribution on wide-belt conveyor (right). The bulk flow of ore pellets circulate in the lower left section of the drum. The fine material adhere to the drum walls and form an irregular surface coating. The middle image show a close-up of the irregular drum surface and coating of fine material around the outlet gaps.

rate 14.4 ton/h. The pile formation is filmed with high-speed cameras, see Fig.8. The average angle of repose of the pile is found to be $\theta_{\mathrm{r}} = 34 \pm 3°$.

5.2. Flow in an inclined drum

The flow inside balling drum RK1 was observed during 30 minutes of stable production of green ore pellets. A camera was placed at the end of the outlet to capture the flow inside the drum , see. Fig. 9. The drum was fed with mass rate $\dot{M}_{\mathrm{RK1}} = 340$ ton/h divided in 110 ton/h iron fines mixed with binding agents and 230 ton/h return feed of undersized material. The drum rotation produce a circulating flow that is nearly stationary and in the rolling or cascading regime [21]. At the bottom of the drum the material form a *plug zone* where ore pellets co-move rigidly with the drum rotation. The material is lifted up to some maximal angle θ_1 where particles begin to slide and form a *shear zone* of a gravity driven flow on top of the plug zone down to the drum bottom at angle θ_2, Fig. 9. The dynamic angle of repose is identified by the surface inclination, i.e., $\theta'_{\mathrm{r}} = 180° - \frac{1}{2}(\theta_1 + \theta_2)$.

From camera measurements it is found $\theta_1 = 120 \pm 2°$, $\theta_2 = 167 \pm 2°$ and $\theta'_{\mathrm{r}} = 35 \pm 5°$. The inclination of the drum also lead to an axial transportation flow, presumably localized to the shear zone. Cloth tracers are dropped into the drum and tracked by camera in order to measure the surface velocity of the

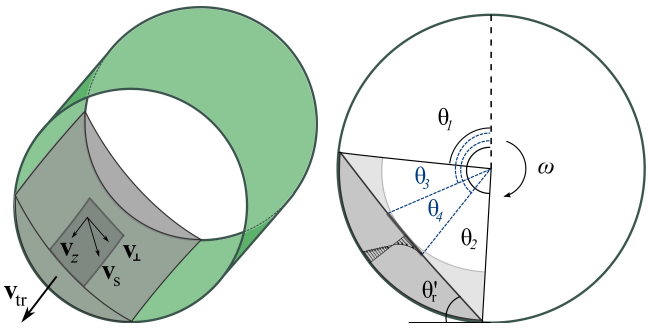

Figure 10: Pellet flow in rotating inclined drum.

bulk flow, v_s, and its axial and cross-sectional components, v_{sz} and $v_{s\perp}$. The measurement region is limited by the angles θ_3 and θ_4 and between the drum center and beginning of the outlet, as indicated in Fig. 10. The measurement results are found in Table 4. The measurement of θ_1 and θ_2 is based on a 100 s recording. The surface velocity is computed by time-of-flight from 10 passages of cloth tracers over the measurement region. We compute the axial bulk transportation velocity as $v_{tr} = \dot{M}/\rho A\chi$, where $A \in [A_{min}, A_{max}]$ is the bulk cross-section area and χ is the packing ratio. The upper and lower bounds of the cross-section area are determined by assuming either the shape of circle sector or of an annulus sector, both limited by θ_1 and θ_2, see Fig, 10. This give $A_{min} = 0.18$ m^2 and $A_{max} = 0.27$ m^2. The packing ratio is assumed $\chi = 0.7$.

The video material also reveal that the drum interior is not perfectly cylindrical but has a structure of bumps and dimples formed by fine material adhering and loosening from drum interior surface, see Fig. 9. This *drum texture* presumably lead to an increased effective surface friction, higher lifting of the material and induce more flow disturbances.

5.3. Material distribution on wide-belt conveyor

The spatial distribution of material on the wide-belt conveyor depends on the flow structure inside the drum and of the geometric shape of the outlet. The outlet is 2.3 m long and has three spiral shaped gaps. The inner and outer width of the gaps are $e_1 = 4.7d$ and $e_2 = 7.9d$ in the z' direction. We describe the resulting material height profile by $h(y, t - x/v_b)$. The goal is a constant height profile $h(y, t - x/v_b) = h_0$ which is presumed to maximize the efficiency of the roller sieve. The flow of material at the end of the wide-belt conveyor, $x = 0$, is captured using video camera over a time period of 16 s. The height profile is extracted by image analysis using feature matching to localize the conveyor belt and color gradient for tracking the material surface. A sample is shown in

Table 4: Validation of simulated bulk behaviour by comparing with observations in balling circuits.

Test	**Quantity**	**Observation**	**Simulation**
Pile shape	θ_{r}	$34 \pm 3^{\circ}$	$36 \pm 2^{\circ}$
Drum flow	θ'_{r}	$35 \pm 5^{\circ}$	$34 \pm 2^{\circ}$
	v_{tr}	0.20 ± 0.03 m/s	0.22 ± 0.02 m/s
	v_{s}	1.31 ± 0.06 m/s	1.27 ± 0.09 m/s
	v_{sz}	0.58 ± 0.05 m/s	0.49 ± 0.03 m/s
	$v_{s\perp}$	1.18 ± 0.07 m/s	1.17 ± 0.09 m/s
Bed profile RK1	σ_h	0.41	
RK1-o			0.83
RK1-m			0.66
RK1-c			0.46
RK1-ic			0.44
	$\sigma_{h-\bar{h}}$	0	
RK1-o			1.01
RK1-m			0.81
RK1-c			0.54
RK1-ic			0.27
Bed profile RK5	σ_h	0.33	
RK5-o			0.83
RK5-m			0.68
RK5-c			0.42
RK5-ic			0.42
	$\sigma_{h-\bar{h}}$	0	
RK5-o			0.71
RK5-m			0.47
RK5-c			0.35
RK5-ic			0.11

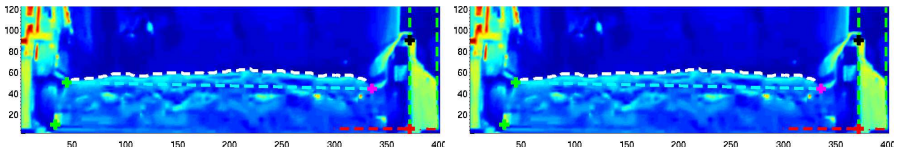

Figure 11: Sample images from extraction of height profile on wide-belt conveyor in RK5.

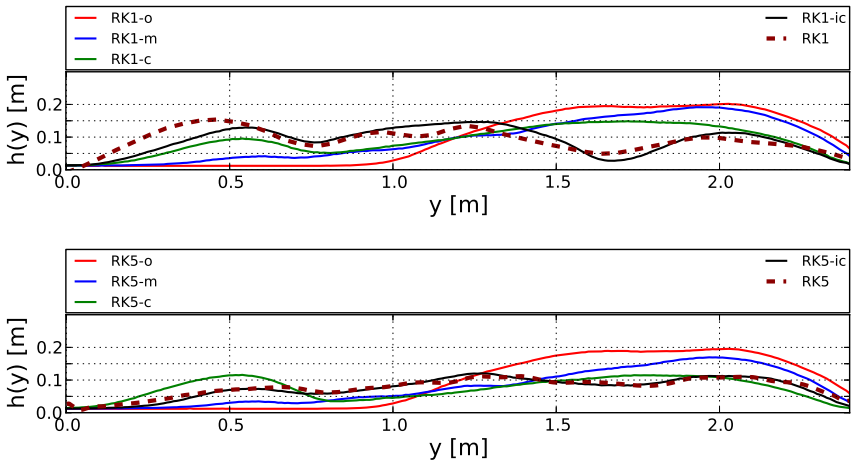

Figure 12: The time averaged height profile on the wide-belt conveyor from RK1 and RK5. The dashed line is the result from video measurement. The solid lines are from simulations using the original outlet (o) , modified outlet (m), with uniform gap coating (c) and with inhomogenous gap coating (ic).

Fig. 11. A 2D height profile $h(y, t - x/v_\mathrm{b})$ is reconstructed for comparison with simulations in Sec. 6. The time averaged profile at $x = 0$ is computed as

$$h(y) = \frac{1}{t_2 - t_1} \int_{t_1}^{t_2} h(y, t) \mathrm{d}t \tag{13}$$

The result from RK1 and RK5 are found in Fig. 12. The coefficient of variation of the height profile is

$$\sigma_h = \sqrt{\frac{1}{w_\mathrm{b}} \int_0^{w_\mathrm{b}} \left[\frac{h(y) - \langle h \rangle}{\langle h \rangle} \right]^2 \mathrm{d}y} \tag{14}$$

where $\langle h \rangle = \frac{1}{w_\mathrm{b}} \int_0^{w_\mathrm{b}} h(y) \mathrm{d}y$ is the average height. The observed values are $\sigma_h^{\mathrm{RK1}} = 0.41$ and $\sigma_h^{\mathrm{RK5}} = 0.33$, which are acceptable although not optimal. The design objective of producing a uniform profile of pellets correspond to $\sigma_h = 0$.

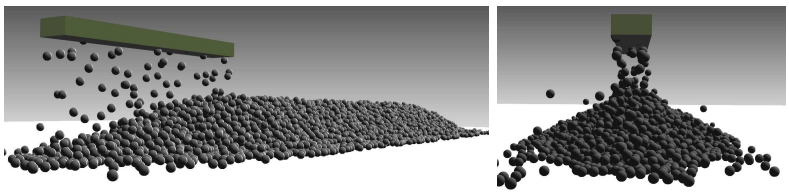

Figure 13: Images from simulation of pile formation.

6. Validation of the simulation model

The observations of ore green pellet flow in the balling circuit described in Sec. 5 are used for validation of simulated bulk behaviour. The validation results are summarized in Table 4. The simulation model is parametrized by the values in Table 1 found from experiments. Monosized particles with diameter d are used. All simulations are performed with time-step $\Delta t = 5$ ms, $N_{\text{it}} = 150$ PGS iterations and $v_{\text{imp}} = 0.05$ m/s, unless otherwise is mentioned. See Sec. 6.4 for an analysis and discussion regarding the choice of time-step. Videos from simulations are found at `http://umit.cs.umu.se/granular/video/`.

6.1. Angle of repose

A long pile is formed by dropping particles at rate 14.4 ton/h from a 0.05×0.4 m^2 source elevated 0.3 m over a planar surface moving 0.1 m/s relative to the source, see Fig. 13. The cross-section profile is measured as the average from 20 segments between $10d$ and $60d$ from the source, see Fig. 14. The average angle of repose is found to be $\theta_{\text{r}} = 36 \pm 2°$. To examine the sensitivity to rolling resistance, the simulation is also performed with rolling resistance coefficient μ_{r} decreased to 10%. The piles disperse more and the resulting angle of repose become 22°. With zero rolling resistance coefficient the initial pile formation has angle of 15° but quickly melt to 0°. Rolling resistance is clearly needed for the formation of piles with correct shape. A simulation with time-step $\Delta t = 0.2$ ms was also made to investigate the effect of errors from large time-step integration. The resulting angle of repose is $33 \pm 2°$. The difference is believed to reside from larger overlap errors occuring at impact in the $\Delta t = 5$ ms simulations. Both results are within the standard variation of the observed angle of repose $34 \pm 3°$.

6.2. Flow in an inclined drum

A virtual replica of the inclined rotating drum is constructed from CAD drawings. The interior drum texture is modeled by perturbing the cylindrical surface with a random distribution of gaussian shaped bumps of width 50 mm and height in the range 30 to 50 mm. The average density of bumps is 20 per m^2. The texture cover also the outlet interior. A particle source is placed at the center of the drum emitting particles of diameter d at a rate $\dot{M}_{\text{RK1}} = 340$ ton/h. The simulation is first run for five evolutions (60 s) to create a nearly

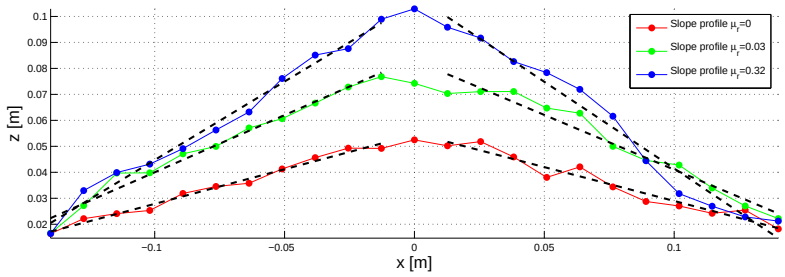

Figure 14: The average pile profile and its linear interpolation for different values of rolling resistance. For $\mu_\mathrm{r} = 0$ the pile quickly disperse to zero angle of repose.

stationary flow, see Fig. 16. The particle dynamics is then captured during one drum evolution, 12 s. The analysis is limited to a 1 m long section centred between the source and the outlet and, for the surface flow, between angles $\theta_3 = 135°$ and $\theta_4 = 160°$. Sample plot of the velocity field and mass density field from a cross-section is shown in Fig. 15 computed by coarse graining on a grid with mesh size of $1d$. The plug zone where material co-rotate rigidly with the drum is clearly visible. The axial transportation occur in the shear zone layer above the plug zone. The surface shape and flow is slightly irregular and nonstationary. The time averaged mass distribution is shown in Fig. 15. The average dynamic angle of repose is found to be $\theta'_\mathrm{r} = 34 \pm 2°$.

The average bulk transportation velocity in the measurement region is 0.22 ± 0.02 m/s. The surface between angles θ_3 and θ_4 is tracked over time and the average surface velocity is found to be $v_\mathrm{s} = 1.27 \pm 0.09$ with cross-sectional and axial components $v_{\mathrm{s}\perp} = 1.17 \pm 0.09$ m/s and $v_{\mathrm{s}z} = 0.49 \pm 0.03$ m/s.

To test the sensitivity to rolling resistance, the simulation is also performed with rolling resistance coefficient μ_r decreased from 0.33 to 0.03. The effect on the flow is significant. The dynamic angle of repose becomes $25 \pm 2°$ and the surface velocity $v_\mathrm{s} = 0.6 \pm 0.1$ with components $v_{\mathrm{s}\perp} = 0.43 \pm 0.1$ m/s and $v_{\mathrm{s}z} = 0.41 \pm 0.03$ m/s. Hence, rolling resistance is a necessary model component also for the simulated drum flow to agree with observations. The effect on the flow by variations of the surface friction, elasticity and particle size was also investigated and found to be small. The time-averaged cross-sectional flow velocities and dynamic angle of repose was affected by roughly 5 % by the changes $\mu'_\mathrm{s} = 0.9\mu_\mathrm{s}$, $E' = 0.5E$, $E' = 2E$ and $d' = 0.8d$.

6.3. Material distribution on wide-belt conveyor

The third validation test is the distribution of ore pellets on the wide-belt conveyor below the drum outlet. This tests the predictive power of NDEM simulation to capture the non-stationary granular flow created by the interaction with a moving irregular geometry. Sample images from simulation is shown in Fig. 16. Simulations are performed both with the original outlet design (RK1-o

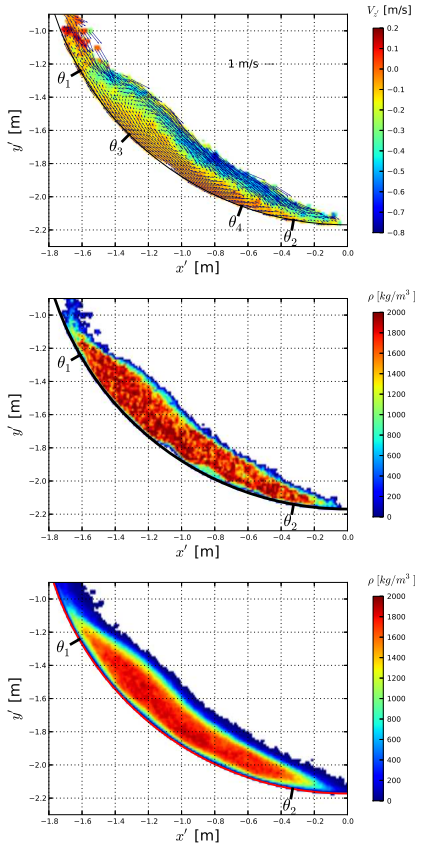

Figure 15: Time instants of flow velocity field (top), mass density field (middle) and time-averaged mass density field (bottom) in a drum cross-section.

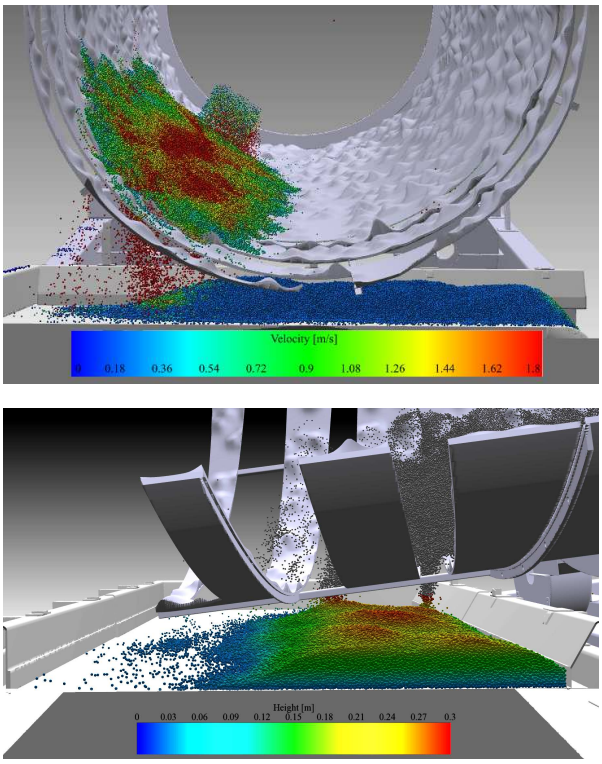

Figure 16: Image from simulation showing material distribution inside drum (top) and on the wide-belt conveyor (bottom). The original outlet deisgn is used. Particles are color coded by velocity and height, respectively.

and RK5-o), in Fig. 2 and 16, with gap width $\{e_1^{\mathrm{o}} : e_2^{\mathrm{o}}\} = \{11.8 : 39.4\}d$, the CAD models of modified outlet that are in operation (RK1 and RK5), see Fig. 7, with $\{e_1^{\mathrm{m}} : e_2^{\mathrm{m}}\} = \{4.7 : 7.9\}d$ as well as outlet geometry models that include coating effect of fine material that make the effective gap width smaller (RK1-c and RK5-c), $\{e_1^{\mathrm{c}} : e_2^{\mathrm{c}}\} = \{3.1 : 6.3\}d$. The gap models are illustrated in Fig. 17.

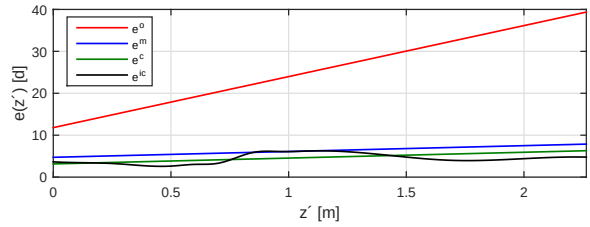

Figure 17: The different outlet gap functions $e(z')$ in RK5 simulations.

First, a stationary flow through the drum is established from a feed of rate $\dot{M}_{\mathrm{RK1}}$. The simulations are then run for three drum evolutions, $t = 36s$, while recording the material distribution on the wide-belt conveyor. The simulations involved nearly 1 M particles for which the total computational time on a 12 cpu machine become of the order 10 hours, see Eq. (8). A sample height surface from the RK5 simulation is found in Fig. 18. The time-averaged profile from RK5 and RK1 is found in Fig. 12 and the coefficients of variation are found in Table 4. To compare the simulated and experimentally measured profiles we compute also the relative coefficient of variation

$$\sigma_{h-\bar{h}} = \sqrt{\frac{4}{w_{\mathrm{b}}} \int_0^{w_{\mathrm{b}}} \left[\frac{h(y) - \bar{h}(y)}{\langle h \rangle + \langle \bar{h} \rangle} \right]^2 \mathrm{d}y} \tag{15}$$

where $h(y)$ is a profile from simulation and $\bar{h}(y)$ is the profile from experimental observation. The simulations confirm that the original outlet model, RK5-o, was indeed a very poor design as it produce a nonuniform profile with almost all material distributed on the right hand side of the wide-belt conveyor and $\sigma_h^{\mathrm{RK5}-o} = 0.83$. But also the simulation with the modified CAD model, RK5-m, distribute a substantial excess of material on the right-hand side. Much more than the experimental observation from balling drums as is seen both in Fig. 18 and 12, and by the value of the relative coefficient of variation $\sigma_{h-\bar{h}}^{\mathrm{RK5-m}} = 0.47$. The clogged outlet geometry, RK5-c, agree better with observation, $\sigma_{h-\bar{h}}^{\mathrm{RK5-c}} = 0.35$, but not entirely. In the region $y \in [1.5, 2.0]$ m the experimental profile show a material depletion that has no correspondence in the simulated profile.

We hypothesize that the material depletion is due to the coating being inhomogeneous and time-dependent. Supposedly, the coating increase gradually as material adheres until it reaches a critical thickness and become too heavy to support its own weight and drop from the outlet. We test this by modifying the gap geometry to an inhomogeneous coating, $e^{\mathrm{ic}}(z')$, as illustrated in

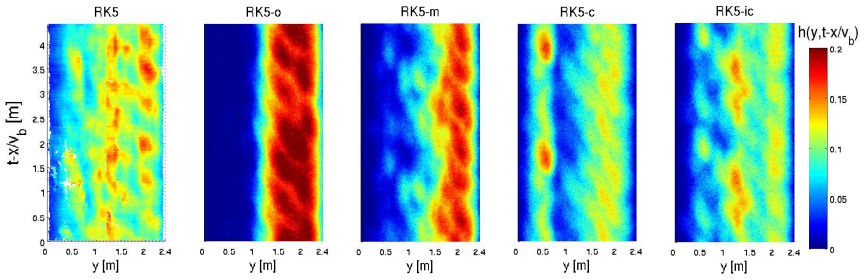

Figure 18: The height surface of the material distribution on the wide-belt conveyor in RK5. Left image is the result from video measurement and the others from simulation. The second to fifth images are from simulations using the original outlet (o) , modified outlet (m), with uniform gap coating (c) and with inhomogenous gap coating (ic).

Fig. 17. The results from the simulations with inhomogeneous gap coating, RK5-ic, match the experimental observations fairly well, $\sigma_{h-\bar{h}}^{\mathrm{RK5-ic}} = 0.11$.

Variations in surface friction, elasticity and particle size were tested to rule out that the deviation in material distribution is mainly due to too imprecise material parameters. The time-averaged bed profile was affected by roughly 5 % by the changes $\mu'_{\mathrm{s}} = 0.9\mu_{\mathrm{s}}$ and $E' = 2E$. The changes $E' = 2E$ and $d' = 0.8d$ affect the bed profile by roughly 15 %. As can be expected, with smaller particles the bed is shifted more to the right. The effect is significant but not enough to explain the deviation from the observed profile. The sensitivity of time-step size is considered in the next subsection.

6.4. Dependency on time-step size

The balling circuit simulations are run with time-step $\Delta t = 5$ ms. This choice is based on the formula Eq. (7) and an assumed impact normal velocity $v_{\mathrm{n}} \sim 0.02$ m/s and error tolerance $\epsilon = 0.01$. This assumed impact velocity is characteristic for flow in a drum with rotation speed $\omega_{\mathrm{d}} = 0.53$ rad/s, causing a characteristic shear rate $\dot{\sigma} \sim 2\omega/[1-cos(\theta/2)]$, where the circular sector angle is $\theta = \theta_2 - \theta_1$. There are impacts with higher contact velocity in the system but we assume the statistical occurrence of these are small and their error contribution to the overall bulk behaviour is insignificant. On the other hand, as found in Sec. 4, using too large time-step may lead to significant errors in the energy dissipation for impacts. Adapting the time-step for high velocity would have severe effects for the computational time. Particles impacting with the pellet bed on the wide-belt conveyor, for instance, have velocity up to $\sqrt{2g_{\mathrm{acc}}h_{\mathrm{db}}} \sim 3$ m/s. The required time-step for maintaining an error tolerance of $\epsilon = 0.01$ for these contacts is 0.04 ms.

The distribution of impact velocity and contact overlap from a simulation with $\Delta t = 5$ ms of material flowing from the drum onto the belt conveyor are presented in histograms in Fig. 19. Analysis show that 7% of the contacts are impacts, i.e., occur with relative normal velocity higher than $v_{\mathrm{imp}} = 0.05$ m/s

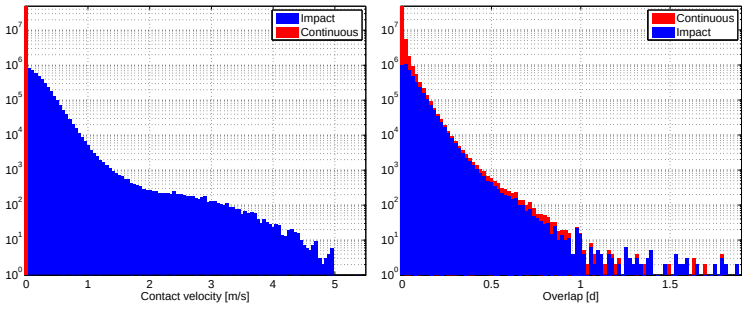

Figure 19: Distribution of normal contact velocity (left) and contact overlap (right) in balling drum and conveyor system from simulation using $\Delta t = 5$ ms. The contacts are divided into continuous contacts (red) and impacts (blue).

and less than 0.01 % has velocity higher than 1 m/s. The majority of contact overlap are below the error tolerance $\epsilon = 0.02$ but 17 % of the contacts have larger overlap. The overlap range up to $2d$, which is consistent with the impact velocity between particles and drum, or conveyor, ranging up to 5 m/s.

To verify the assumption that $\Delta t = 5$ ms is indeed a valid time-step and that the errors from high-velocity contacts do not have a significant contribution to the bulk behaviour, a simulation was also run with time-step $\Delta t = 0.1$ ms. The drum flow characteristics are $\theta'_{\mathrm{r}} = 33 \pm 2°$, $v_{\mathrm{tr}} = 0.23 \pm 0.03$ m/s, $v_{\mathrm{s}} = 1.0 \pm 0.1$, $v_{\mathrm{sz}} = 0.45 \pm 0.03$ m/s and $v_{s\perp} = 0.9 \pm 0.1$ m/s for the RK1. This is in good agreement with both the experimental observation and with the $\Delta t = 5$ ms simulations in Table 4. Histograms of the contact normal velocity and overlap from the $\Delta t = 0.1$ ms simulation is found in Fig. 20. At finer time-discretization more contact events can be resolved in time. The impact threshold $v_{\mathrm{imp}} = \epsilon d/\Delta t$ become roughly 2.5 m/s, i.e., essentially all contacts are resolved as continuous contacts. Furthermore, in this regime the time-step is small enough for the normal contact dissipation to be resolved with the physical viscosity from Hertz contact law, i.e., $\tau_{\mathrm{n}} = \max(n_{\mathrm{s}}\Delta t, \varepsilon_{\mathrm{n}}/\gamma_{\mathrm{n}})$ become $\varepsilon_{\mathrm{n}}/\gamma_{\mathrm{n}} = c/e_{\mathrm{H}}$. We identified $c \approx 1$ ms, from the high-speed camera measurements in Fig. 4. These adjustments of v_{imp} and τ_{n} with time-step are important. Otherwise the small time-step simulation model become too dissipative and produce a flow that does not agree well with observations.

7. Conclusions

A successful parameterization, verification and validation of a NDEM model for iron ore green pellets for the design and control of balling circuits has been demonstrated. The parameterization consists in the direct identification of individual ore green pellet physical parameters. The procedure involves no parameter calibration. The simulated bulk behaviour in the formation of piles and flow in a rotating inclined drum agrees with camera-based measurements in the

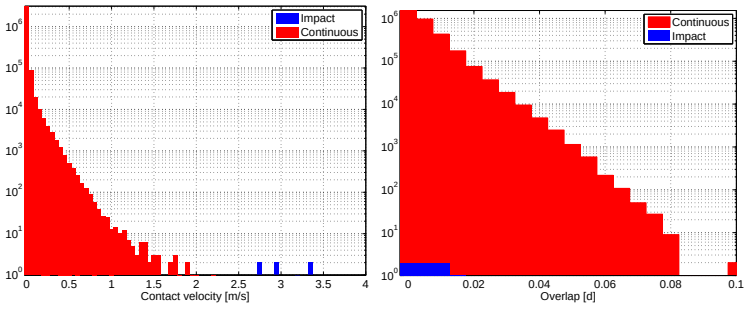

Figure 20: Distribution of normal contact velocity (left) and contact overlap (right) in balling drum and conveyor system from simulation using $\Delta t = 0.1$ ms. The contacts are divided into continuous contacts (red) and impacts (blue).

pelletizing plant. The angle of repose agrees within 5% and the flow velocity within 10 %. The pellet distribution on the wide-belt conveyor from the drum outlet show a more significant discrepancy between simulation and real system. The proposed explanation is that the simulated and actual outlet geometry do not agree although they are based on the same CAD model. Observations reveals that fine material adheres to the inside of the drum and outlet, creating a thick coating that alters the geometry. In particular, the outlet gaps become more narrow. Simulations confirm that the outlet flow is sensitive to this effect and that the material distribution produced by outlet geometries where this is included agree better with observation. The coating is believed to be dynamic in nature, gradually increasing in thickness until it breaks and drop, making the outlet gap narrowing variable and inhomogeneous. This has the consequence that even if a stationary flow inside the drum can be achieved, the material distribution on wide-belt conveyor and roller sieve will nevertheless have variations. The conclusion is that the outlet should be designed with materials and geometric shape which minimize the amount of coating or at least minimize the variability and effect on the flow.

The sensitivity of the simulation model to parameters is also investigated. It is shown that the rolling resistance is a necessary component of the model to obtain stable piles and the rolling resistance coefficient significantly affect the shape of piles as well as the flow characteristics in the rotating drum. The drum flow is found not to be sensitive to particle size. For an accurate conveyor bed profile beneath the outlet the detailed outlet geometry and rolling resistance are the critical parameters, but next to this the particle size was also found to be important.

It is also demonstrated that using time-step as large as 5 ms do not cause any statistically significant errors to the bulk behaviour as compared to using 0.1 ms although the larger time-step occasionally produce large errors in contacts between individual particles. As contrast, a conventional DEM simulation would require a time-step of size $\Delta t_{\mathrm{DEM}} \leq 0.17\sqrt{m/k_{\mathrm{n}}}$ [22], which evaluates to 0.02

ms for the given material parameters. Hence, NDEM simulation provide a time-efficient and reliable tool for exploring and optimizing the design and control of iron ore pellet balling drums and of similar systems. Future work should include extension to nonuniform and variable size distribution of ore green pellets and modeling of the mixing with ore slurry and the agglomeration process inside the drum.

Acknowledgements

This project was supported by Algoryx Simulations, LKAB, UMIT Research Lab and VINNOVA (dnr 2012-01235, 2014-01901).

Appendix

A. Simulation algorithm

The algoritm for simulating a system of granular material using NDEM with PGS solver is given in Algorithm 1. The projection on line 14 limit the

Algorithm 1 NDEM simulation with PGS solver

1: constants and parameters
2: initialization: $(\mathbf{x}_0, \mathbf{v}_0)$
3: **for** $i = 0, 1, 2, \ldots, t/\Delta t$ **do** ▷ Time stepping
4: contact detection
5: compute $\mathbf{g}, \mathbf{G}, \boldsymbol{\Sigma}, \boldsymbol{\Upsilon}, \mathbf{D}$, see Eq. (18)
6: impact stage PGS solve $\mathbf{v}_i \to (\mathbf{v}_i^+, \boldsymbol{\lambda}_i^+)$
7: $\mathbf{b}_\mathrm{n} = -(4/\Delta t)\boldsymbol{\Upsilon}_\mathrm{n}\mathbf{g}_\mathrm{n} + \boldsymbol{\Upsilon}_\mathrm{n}\mathbf{G}_\mathrm{n}\mathbf{v}_i^+$
8: pre-step $\mathbf{v} = \mathbf{v}_i^+ + \Delta t \mathbf{M}^{-1}\mathbf{f}_\mathrm{ext}$
9: **for** $k = 0, 1, \ldots, N_\mathrm{it} - 1$ or $|\mathbf{r}| \leq r_\mathrm{min}$ **do** ▷ PGS iteration
10: **for** each contact $\alpha = 0, 1, \ldots, N_\mathrm{c} - 1$ **do**
11: **for** each constraint n of contact α **do**
12: $\mathbf{r}_{n,k}^{(\alpha)} = -\mathbf{b}_{n,k}^{(\alpha)} + \mathbf{G}_n^{(\alpha)}\mathbf{v}$ ▷ residual
13: $\boldsymbol{\lambda}_{n,k}^{(\alpha)} = \boldsymbol{\lambda}_{n,k-1}^{(\alpha)} + \mathbf{D}_{n,(\alpha)}^{-1}\mathbf{r}_{n,k}^{(\alpha)}$ ▷ multiplier
14: $\mathrm{proj}(\boldsymbol{\lambda}_{n,k}^{(\alpha)}, \mathbf{v}) \to \boldsymbol{\lambda}_{n,k}^{(\alpha)}$ ▷ project
15: $\Delta\boldsymbol{\lambda}_{n,k}^{(\alpha)} = \boldsymbol{\lambda}_{n,k}^{(\alpha)} - \boldsymbol{\lambda}_{n,k-1}^{(\alpha)}$
16: $\mathbf{v} = \mathbf{v} + \mathbf{M}^{-1}\mathbf{G}_{n,(\alpha)}^T \Delta\boldsymbol{\lambda}_{n,k}^{(\alpha)}$
17: **end for**
18: **end for**
19: **end for**
20: $\mathbf{v}_{i+1} = \mathbf{v}$ ▷ velocity update
21: $\mathbf{x}_{i+1} = \mathbf{x}_i + \Delta t \mathbf{v}_{i+1}$ ▷ position update
22: **end for**

multipliers to the Signorini-Coulomb law. Each contact α between body a and

b add contributions to the constraint vector and normal and friction Jacobians according to

$$
\begin{aligned}
\delta_{(\alpha)} &= \mathbf{n}_{(\alpha)}^{\mathrm{T}}(\mathbf{x}_a + \mathbf{d}_a^{(\alpha)} - \mathbf{x}_b - \mathbf{d}_b^{(\alpha)}) \\
g_{(\alpha)} &= \delta_{(\alpha)}^{e_{\mathrm{H}}} \\
\mathbf{G}_{\mathrm{n}a}^{(\alpha)} &= e_{\mathrm{H}} g_{(\alpha)}^{e_{\mathrm{H}}-1} \left[\begin{array}{cc} -\mathbf{n}_{(\alpha)}^{\mathrm{T}} & -(\mathbf{d}_a^{(\alpha)} \times \mathbf{n}_{(\alpha)})^{\mathrm{T}} \end{array} \right] \\
\mathbf{G}_{\mathrm{n}b}^{(\alpha)} &= e_{\mathrm{H}} g_{(\alpha)}^{e_{\mathrm{H}}-1} \left[\begin{array}{cc} \mathbf{n}_{(\alpha)}^{\mathrm{T}} & (\mathbf{d}_b^{(\alpha)} \times \mathbf{n}_{(\alpha)})^{\mathrm{T}} \end{array} \right] \\
\mathbf{G}_{\mathrm{t}a}^{(\alpha)} &= \left[\begin{array}{cc} -\mathbf{t}_1^{(\alpha)\mathrm{T}} & -(\mathbf{d}_a^{(\alpha)} \times \mathbf{t}_1^{(\alpha)})^{\mathrm{T}} \\ -\mathbf{t}_2^{(\alpha)\mathrm{T}} & -(\mathbf{d}_a^{(\alpha)} \times \mathbf{t}_2^{(\alpha)})^{\mathrm{T}} \end{array} \right] \\
\mathbf{G}_{\mathrm{t}b}^{(\alpha)} &= \left[\begin{array}{cc} \mathbf{t}_1^{(\alpha)\mathrm{T}} & (\mathbf{d}_b^{(\alpha)} \times \mathbf{t}_1^{(\alpha)})^{\mathrm{T}} \\ \mathbf{t}_2^{(\alpha)\mathrm{T}} & (\mathbf{d}_b^{(\alpha)} \times \mathbf{t}_2^{(\alpha)})^{\mathrm{T}} \end{array} \right]
\end{aligned}
\tag{16}
$$

The diagonal matrices and Schur complement matrix $\mathbf{D}$ are

$$
\begin{aligned}
\mathbf{\Sigma}_{\mathrm{n}} &= \frac{4}{\Delta t^2} \frac{\varepsilon_{\mathrm{n}}}{1 + 4\frac{\tau_{\mathrm{n}}}{\Delta t}} \mathbf{1}_{N_c \times N_c} \\
\mathbf{\Sigma}_{\mathrm{t}} &= \frac{\gamma_{\mathrm{t}}}{\Delta t} \mathbf{1}_{2N_c \times 2N_c} \\
\mathbf{\Sigma}_{\mathrm{r}} &= \frac{\gamma_{\mathrm{r}}}{\Delta t} \mathbf{1}_{3N_c \times 3N_c} \\
\mathbf{\Upsilon}_{\mathrm{n}} &= \frac{1}{1 + 4\frac{\tau_{\mathrm{n}}}{\Delta t}} \mathbf{1}_{N_c \times N_c} \\
\mathbf{D} &= \mathbf{G}\mathbf{M}^{-1}\mathbf{G}^T + \mathbf{\Sigma}
\end{aligned}
\tag{17}
$$

The mapping between regularization parameters and material parameters are

$$
\begin{aligned}
\varepsilon_{\mathrm{n}} &= e_{\mathrm{H}}/k_{\mathrm{n}} = 3e_{\mathrm{H}}(1-\nu^2)/E\sqrt{r^*} \\
\tau_{\mathrm{n}} &= \max(n_{\mathrm{s}}\Delta t, \varepsilon_{\mathrm{n}}/\gamma_{\mathrm{n}}) \\
\gamma_{\mathrm{n}}^{-1} &= k_{\mathrm{n}} c/e_{\mathrm{H}}^2
\end{aligned}
\tag{18}
$$

and we use $\gamma_{\mathrm{t}} = \gamma_{\mathrm{r}} = 10^{-6}$, $n_{\mathrm{s}} = 2$.

References

[1] F. Radjai, V. Richefeu, Contact dynamics as a nonsmooth discrete element method, Mechanics of Materials 41 (6) (2009) 715–728.

[2] M. Servin, D. Wang, C. Lacoursière, K. Bodin, Examining the smooth and nonsmooth discrete element approach to granular matter, Int. J. Numer. Meth. Engng. 97 (2014) 878–902.

[3] D. Wang, M. Servin, K.-O. Mickelsson, Outlet design optimization based on large-scale nonsmooth DEM simulation, Powder Technology 253 (0) (2014) 438–443.

[4] S. Forsmo, Influence of green pellet properties on pelletizing of magnetite iron ore, Ph.D. thesis, Luleå University of Technology, Luleå (2007).

[5] I. Cameron, F. Wang, C. Immanuel, F. Stepanek, Process systems modelling and applications in granulation: A review, Chemical Engineering Science 60 (14) (2005) 3723–3750.

[6] R. Soda, A. Sato, J. Kano, E. Kasai, F. Saito, M. Hara, T. Kawaguchi, Analysis of granules behavior in continuous drum mixer by DEM, ISIJ International 49 (5) (2009) 645–649.

[7] T. Pöschel, T. Schwager, Computational Granular Dynamics, Models and Algorithms, Springer-Verlag, 2005.

[8] J. J. Moreau, Numerical aspects of the sweeping process, Computer Methods in Applied Mechanics and Engineering 177 (1999) 329–349.

[9] M. Jean, The non-smooth contact dynamics method, Computer Methods in Applied Mechanics and Engineering 177 (1999) 235–257.

[10] F. A. Bornemann, C. Schütte, Homogenization of Hamiltonian systems with a strong constraining potential, Phys. D 102 (1-2) (1997) 57–77.

[11] N. V. Brilliantov, F. Spahn, J.-M. Hertzsch, T. Pöschel, Model for collisions in granular gases, Phys. Rev. E 53 (1996) 5382–5392.

[12] C. Lacoursière, Regularized, stabilized, variational methods for multibodies, in: D. F. Peter Bunus, C. Führer (Eds.), The 48th Scandinavian Conference on Simulation and Modeling (SIMS 2007), Linköping University Electronic Press, 2007, pp. 40–48.

[13] K. G. Murty, Linear Complementarity, Linear and Nonlinear Programming, Helderman-Verlag, Heidelberg, 1988.

[14] Algoryx Simulations. AGX Dynamics, December 2014.

[15] J. Ai, J.-F. Chen, J. M. Rotter, J. Y. Ooi, Assessment of rolling resistance models in discrete element simulations, Powder Technology 206 (3) (2011) 269–282.

[16] N. Estrada, E. Azéma, F. Radjai, A. Taboada, Identification of rolling resistance as a shape parameter in sheared granular media, Phys. Rev. E 84 (2011) 011306.

[17] N. Estrada, A. Taboada, F. Radjaï, Shear strength and force transmission in granular media with rolling resistance, Phys. Rev. E 78 (2008) 021301.

[18] J. Huang, M. V. da Silva, K. Krabbenhoft, Three-dimensional granular contact dynamics with rolling resistance, Computers and Geotechnics 49 (0) (2013) 289–298.

[19] A. Tasora, M. Anitescu, A complementarity-based rolling friction model for rigid contacts, Meccanica 48 (7) (2013) 1643–1659.

[20] S. Forsmo, P.-O. Samskog, B. Björkman, A study on plasticity and compression strength in wet iron ore green pellets related to real process variations in raw material fineness, Powder Technology 181 (3) (2008) 321–330.

[21] H.-T. Chou, C.-F. Lee, Cross-sectional and axial flow characteristics of dry granular material in rotating drums, Granular Matter 11 (1) (2008) 13–32.

[22] C. O. J. Bray, Selecting a suitable time step for discrete element simulations that use the central difference time integration scheme, Engineering Computations 21 (2/3/4) (2004) 278–303.